Vacuum 180 (2020) 109583

Contents lists available at ScienceDirect

Vacuum

journal homepage: http://www.elsevier.com/locate/vacuum

Effects of yttrium doping on helium behavior in zirconium hydride films

Zhibin Han [a,b], Ludan Zhang [c,*], Chunjie Wang [b], Xiaojie Ni [d], Bangjiao Ye [d], Liqun Shi [b,**]

[a] School of Electronic and Computer Engineering, Peking University Shenzhen Graduate School, Shenzhen, 518055, China
[b] Department of Nuclear Science and Technology, Fudan University, Shanghai 200433, China
[c] School of Biological and Chemical Sciences, Queen Mary University of London, Mile End Road, London, E1 4NS, UK
[d] State Key Laboratory of Particle Detection and Electronics, University of Science and Technology of China, Hefei, 230026, China

ARTICLE INFO

Keywords:
Yttrium-doped
Helium behaviors
Hydrogen storage

ABSTRACT

The zirconium hydride alloy films with different yttrium concentration were prepared by magnetron sputtering and studied using ion beam analysis (IBA), X-ray diffraction (XRD), thermal desorption spectrometry (TDS), positron annihilation spectroscopy (PAS) and nanoindentation. It was found that the yttrium atom, which is originally insoluble in zirconium metal, can largely dissolve in the zirconium hydride matrix through the introduction of hydrogen. The helium thermal desorption experiment shows that as the doped amount of yttrium atoms increases, a large number of helium atoms will be released in the form of helium bubbles at the grain boundaries in the matrix at *ca.* 900K. Combined with XRD results, it is concluded that as the yttrium atoms are introduced, more grain boundaries will form in the zirconium hydride matrix. These grain boundaries act as crystal defects, which have a strong trapping effect on helium atoms, causing a large number of helium bubbles to aggregate at the grain boundaries in the matrix. In addition, it is noteworthy that yttrium doping can increase the hardness and elastic modulus of zirconium hydride.

1. Introduction

Tritium, an important hydrogen isotope, is an important raw material for future fusion energy production [1]. The massive storage of tritium is always an important research topic in the nuclear industry. However, due to its radioactivity and high diffusion coefficient, the traditional hydraulic gas storage method cannot meet the storage requirements of tritium. Correspondingly, metal tritides have attracted massive attention as a tritium storage method due to their low-radioactivity, low equilibrium pressure, large storage capacity and high stability in air. Compared with the conventional metals such as U, Pt, La–Ni–Al, etc., zirconium has become a hot spot for metal tritide research due to its advantages of no radioactivity, low cost and large storage capacity. As a β-decay nuclide, tritium can decay into helium-3 spontaneously with a half-life period of 12.3 years [2]. The helium-3 atom (inert gas) is difficult to dissolve in the metal matrix because its outer shell electron orbital is fully occupied. Therefore, the accumulation of large amount of helium atoms in the material can cause the metal tritide to swell and flake [3–5]. This kind of material deterioration phenomenon is also called helium embrittlement [6,7]. As a result, the condition of the helium inclusions in metal tritide determines the usage lifetime of the tritium storage material directly.

In order to reduce the influence of helium embrittlement on zirconium tritide, some zirconium alloys such as Zr–Co, Zr–Y, Zr–Ti, etc. have been studied [8–12]. Compared with pure Zr metal, Zr–Y alloy exhibits good properties in terms of corrosion resistance and hydrogen embrittlement resistance [9,10]. Li et al. found that the doped yttrium element formed the oxide precipitation phase in the pure zirconium matrix. Due to the strong affinity of yttrium for hydrogen, zirconium hydride tends to nucleate and grow within the grains rather than at the grain boundaries, which results in the observed preferential distribution of hydrides within the grains. This indicates that hydrogen embrittlement in the matrix can be reduced by reducing the size of the precipitated hydride and preferential intra-particle hydride distribution can be realized [11]. Meanwhile, it was found that the introduction of the precipitate phase can inhibit the migration and aggregation of the helium bubbles. The huge difference between the crystal lattice of the precipitate and the metal will generate a local deformation field in the matrix. There is a high density of interface dislocations in the deformation field, which can be used as an effective helium trap. Through the high bubble trapping

* Corresponding author.
** Corresponding author.
E-mail addresses: ludan.zhang@qmul.ac.uk (L. Zhang), lqshi@fudan.edu.cn (L. Shi).

https://doi.org/10.1016/j.vacuum.2020.109583
Received 31 January 2020; Received in revised form 21 June 2020; Accepted 22 June 2020
Available online 2 July 2020

ability, the dispersion of this discontinuous precipitate inside the grains helps to effectively suppress the transport of helium atoms from the inside of the grains to the grain boundaries [12]. However, the crystal structures of the Zr–Y system and the Zr–Y–H system are quite different. Therefore, it is necessary to study the helium behavior in Zr–Y–H system.

In this work, we investigated the effect of different yttrium doping amounts on the helium behavior in zirconium hydride films. Through the X-ray diffraction (XRD) experiment, it is found that with the introduction of hydrogen, the yttrium atoms that are originally insoluble in the zirconium matrix can largely dissolve in zirconium hydride. As the doping amount of yttrium increases, the crystallinity of zirconium hydride decreases significantly. Through the thermal desorption experiment, it is found the existence of yttrium causes the release of helium in a large scale at *ca.* 900K, which corresponds to the helium state at the grain boundaries of zirconium hydride. It indicates that as the yttrium doping amount increases, more grain boundaries are formed, and these grain boundaries have a strong trapping effect on helium atoms. In this work, considering the radioactivity of tritium and helium-3, we used hydrogen and helium-4 instead of tritium and helium-3 based on their same electronic structure and similar chemical properties.

2. Experimental

2.1. Specimens preparation

The pure and Y-doped zirconium hydride films were deposited on silicon and molybdenum substrates through a DC magnetron sputtering system. Both of the silicon and molybdenum substrates were cleaned ultrasonically before use. A pure zirconium target, on which some pure yttrium pieces were distributed evenly, was used for sputtering. The maximum elevated temperature of the sample is less than 70 °C. The sputtering atmosphere used in the deposition process was a mixture of pure hydrogen, helium and argon. The gas flows of the argon, helium and hydrogen in the mixture were controlled by three gas flowmeters. The base pressure of the chamber before sputtering was less than 1×10^{-5} Pa. The sputtering pressure and power were 0.8 Pa and 90 W respectively and all films were deposited for 80 min.

2.2. Characterization

Ion beam analysis (IBA) with proton induced X-ray emission (PIXE) and elastic recoil detection analysis (ERDA) were employed to determine the concentrations of yttrium and light elements (hydrogen and helium) respectively at the NEC 95DH- 2 × 3 MeV pelletron tandem accelerator of Fudan University. A 3.0 MeV collimated proton beam was used in the PIXE measurement. The depth profiles of the light elements (hydrogen and helium) were measured simultaneously by using 8.5 MeV carbon ions with elastic recoil detection analysis [13]. The atomic concentration distributions for hydrogen and helium ([H or He]/[Ti] × 100 at.%) were derived from the ERD spectra by Alegria 1.2 code [14].

The crystal structure of the samples was characterized by X-ray diffraction (XRD) at a D8 ADVANCE and DAVINCI.DESIGN X-ray diffractometer made by Bruker. The thermal desorption spectrometry was used for the investigation of the interaction between helium and the defects in the samples. The samples mounted in a molybdenum crucible were heated using a linear temperature ramp from room temperature to 1773K at a rate of 1 K/s. The TDS analysis was performed using an RGA200 residual gas analyzer manufactured by Stanford Research Systems Co. The measured mass range is 1–200 amu. The resolution is better than 0.5 amu at 10% peak height. The minimum detectable partial pressure is 5×10^{-11} Torr. The sample defect profiles were characterized by positron annihilation spectroscopy (PAS). The mechanical properties (hardness and elastic modulus) of the films were characterized using the nanoindenter G200 from the Agilent corporation (America). The indenter of nanoindenter was equipped with a diamond Berkovich indenter (triangular based pyramid) and the maximum load of this indenter was 500 mN.

3. Results and discussion

3.1. Structural characterization of Y-doped zirconium hydride films

The thickness of the Y-doped ZrH_2 films measured by Rutherford Backscattering Spectrometry (RBS) was about 2 μm, and the corresponding RBS spectrum was shown in Fig. 1 [15]. Since the atomic masses of the yttrium and zirconium are very close to each other (difference in mass is only 2.5%), the yttrium peak can not be discerned on the RBS spectrum. Therefore, the doping amount of yttrium is measured using PIXE. Fig. 2 shows the PIXE spectrum of the zirconium hydride film with and without 9% Y doping. It can be seen that there are two obvious X-ray peaks in the samples doped with yttrium. The two new X-ray peaks were characteristic K_α (14.92 eV) and K_β (16.73 eV) X-rays from Y element [16]. After background fitting and subtraction using the GUPIX-96 code [17], a net count of characteristic X-ray peaks was obtained. Reference sample GSD-6 (the elemental content of which has been analyzed by the ICP method) is used to determine the PIXE parameters. The concentrations of yttrium in ZrH_2 films ([Y]/([Y]+[Zr]) × 100 at.%) were determined to be 4% and 9%, which were hereafter denoted as 4%Y films and 9%Y films respectively. The concentration of helium and hydrogen in the films was determined using ERD analysis. The depth profile of helium in the films is shown in Fig. 3, which shows that the helium in the film is evenly distributed in the sample and the content is about 9 at.% ([He]:[Zr] × 100 at.%) [18]. The hydrogen concentration in the sample is about 200 at.%, which suggests that the zirconium in the films mainly exists as ZrH_2.

In order to study the effect of yttrium doping on zirconium hydride, we performed XRD analysis on pure Zr, Zr–4%Y alloy and 4%Y doped zirconium hydride films (simplified as Zr, Zr–4Y and Zr–4YH), as is shown in Fig. 4. By comparing the diffraction peaks of the pure zirconium sample with the standard PDF card, the diffraction peaks at 2θ of 31.62° and 34.52° correspond to the (100) and (102) lattice planes of α-Zr, respectively [19]. For Zr–4Y alloy, three main diffraction peaks appear in the diffraction pattern. Both zirconium and yttrium in the Zr–4Y alloy have good crystallinity and no dissolution of yttrium occurs. To be specific, the diffraction peak with 2θ of 28.42° corresponds to the (111) lattice plane of Y_2O_3 for Zr–4Y alloy [20]. It is because that the yttrium atoms react with oxygen easily, some of them are present as Y_2O_3 in the sample after doping. After the introduction of hydrogen to Zr–4Y alloy, no relevant diffraction peaks of yttrium were found in the

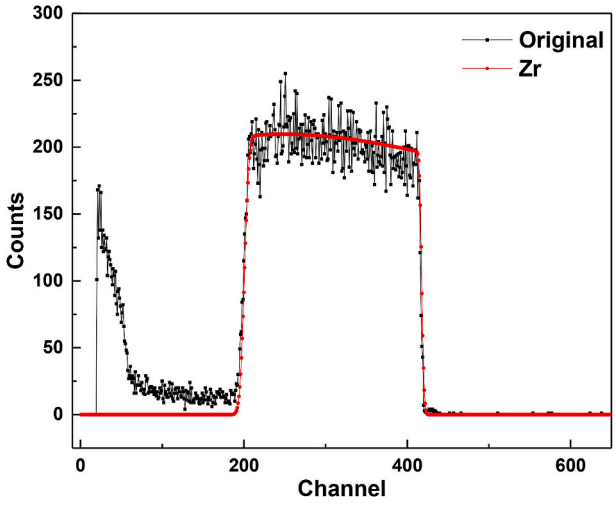

Fig. 1. The RBS spectra of Y-doped ZrH_2 film deposited on Si substrate using 3.8 MeV ^{4}He ion beam. The scattering angle is 165°.

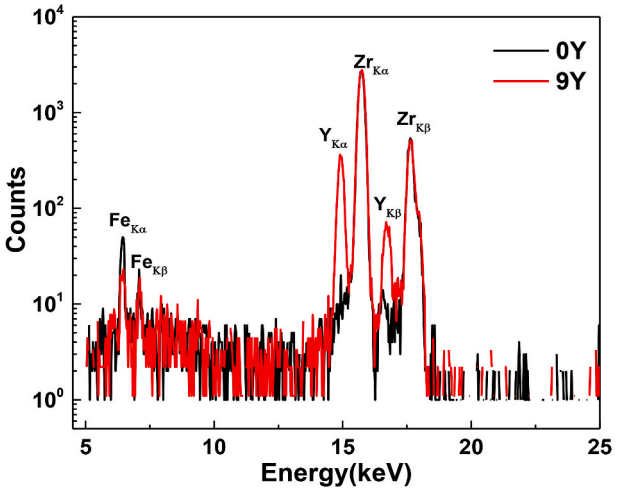

Fig. 2. The PIXE spectra of ZrH_2 and Y-doped ZrH_2 film deposited on Si substrate using 2.0 MeV proton ion beam.

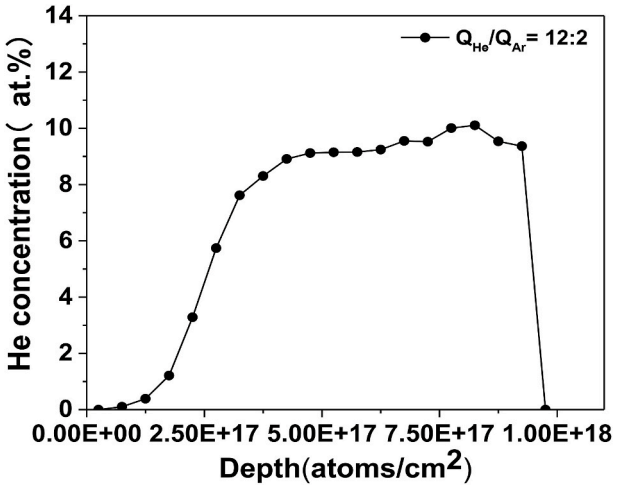

Fig. 3. Helium depth profile of 9%Y doped ZrH_2 film deposited on Si substrates at 0.8 Pa with relative helium flow rate $Q_{He}/Q_{Ar} = 12 : 2$.

XRD pattern for Zr–4YH sample in Fig. 4. Instead, the diffraction pattern only shows the diffraction peak of (111) lattice plane at 2θ of 31.85° for ZrH_2 with the face-centered cubic structure [21]. XPS and TEM were employed to investigate the yttrium-doped metal hydride in our previous work [22]. The XPS result indicates that in the film matrix, the Y element mainly exists in the form of Y_2O_3 and YH_2. Due to the surface oxidation, 92% yttrium exists in the form of Y_2O_3 in the surface oxidation layer while only 44% yttrium exists in the form of Y_2O_3 in the bulk, and the remaining Y reacts with the H within the matrix to form YH_2. The HAADF-STEM measurements prove that the Y element exists in the form of yttrium oxide after annealing.

The X-ray diffraction patterns of the helium-containing zirconium hydride films with different yttrium doping amounts are shown in Fig. 5, where the amount of helium is 9 at.% for all. The substrates used for the ZrYHHe films were molybdenum substrates. By comparing the standard PDF diffraction cards, it can be known that the diffraction peaks for 2θ of 40.5° and 58.5° correspond to the (110) and (200) lattice planes of molybdenum in Fig. 5 [23]. The diffraction peaks of 2θ at 31.5° and 51.65° correspond to the (111) and (220) lattice planes of ZrH_2, respectively. As the yttrium doping concentration increases, the preferred orientation of the zirconium hydride changes in these samples. The preferred diffraction peak changes from the original (111) lattice

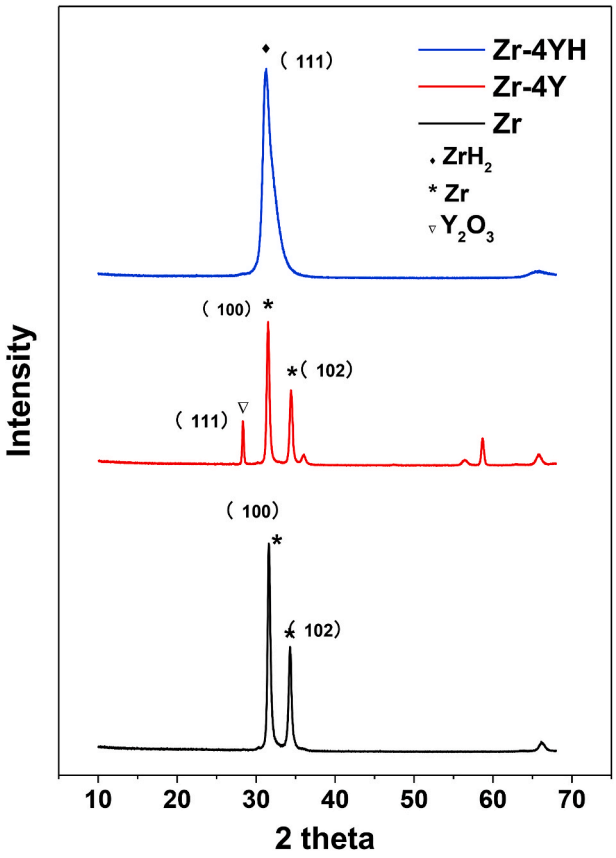

Fig. 4. XRD patterns of Zr, Zr+4%Y and ZrH_2+4%Y films deposited on Si substrates at 0.8 Pa.

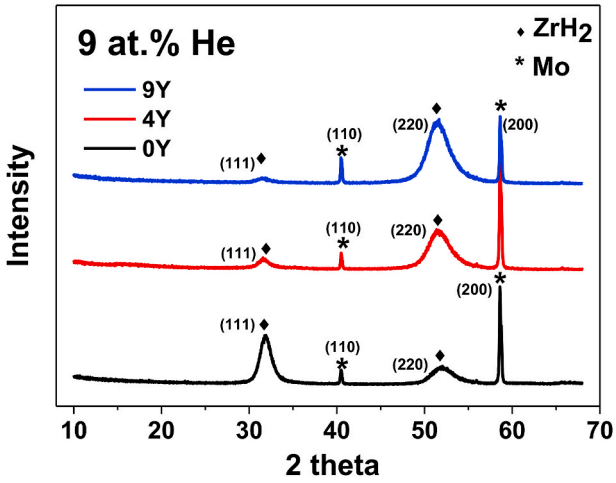

Fig. 5. XRD patterns of ZrH_2 and Y-doped ZrH_2 films with about 9 at.% helium deposited on Mo substrates at 0.8 Pa.

plane to the (220) lattice plane. The work on yttrium-doping titanium hydride film has a similar phenomenon [24]. What is different is that the incorporation of yttrium into the titanium hydride causes a significant lattice expansion. Here in this work since the atomic size of the yttrium atom dissolved in zirconium hydride is very close to that of zirconium, the doping of yttrium does not cause obvious lattice expansion in the diffraction patterns.

3.2. Thermal helium desorption spectrometry of Y-doped zirconium hydride films

In order to study the effect of helium on zirconium hydride with and without yttrium, we performed TDS analysis, as is shown in Fig. 7. According to the first adsorption model [25], the trapped helium states based on different thermal desorption peaks can be calculated by Eq. (1), where N is the number of desorbed helium atoms from the sample, ν is the attempt frequency of atoms in crystal ($\nu \approx 1 \times 10^{13}$/s), E is the dissociation energy, k is the Boltzmann constant, and T is absolute temperature.

$$\frac{E}{kT^2} = \frac{\upsilon}{\beta}\exp\left(\frac{E}{kT}\right). \quad (1)$$

Based on Eq. (1), the dissociation energy of helium atoms that corresponds to different desorption peaks can be calculated, and the values are shown on the top axis in Fig. 7. In this work, the thermal desorption curves can be divided into three main regions, representing three different helium bound states in yttrium-doped ZrH_2 films [26–28]. To be specific, zone I, II, and III correspond to temperatures below 800K, 800K–1100K, and 1100K–1775K respectively.

3.3. Discussion

In order to understand the desorption condition of different components within the yttrium-doped ZrH_2 alloy films with about 9 at.% helium, the thermal desorption spectra in vacuum of these components of different mass were analyzed, as shown in Fig. 6. The thermal desorption spectrum of mass = 18 shows an obvious desorption peak at ca. 367 K in which the mass corresponds to H_2O and the desorption temperature of H_2O is 367 K. Similarly, the thermal desorption spectra of mass = 2 and mass = 4 correspond to the H_2 and He within the helium-contained ZrH_2 alloy films, respectively. For H_2, with the increasement of the temperature, the desorption peak over the range of 600 K–800 K represents the release of H_2, which indicates the decomposition of ZrH_2 accompanied by the phase transition from the fcc structure to hexagonal close-packed structure. Through comparing the desorption spectra of H_2O, H_2 and He, it can also be inferred that the desorption condition of He is not affected by the previously released H_2O and He. The helium thermal desorption spectrum of ZrH_2 without yttrium doping is shown in Fig. 7a. The helium release mainly occurs in Zone III, which indicates that the yttrium in the ZrH_2 film mainly forms helium bubbles inside the matrix before the yttrium doping. During the deposition of ZrH_2 films in the plasma, helium atoms are uniformly implanted into the film by backscattering with the zirconium target. These helium atoms preferentially combine with crystal defects such as vacancies in the film to form helium-vacancy complexes (He_nV_m). At the same time, the interstitial helium atoms have a low activation energy of about 0.4 eV and have a tendency to aggregate with each other, so the interstitial helium atoms will move to the helium-vacancy complexes or sink with the adjacent helium atoms as self-interstitials (SIAs) [29,30]. With the accumulation of helium atoms, bubbles with different sizes will form in the lattice, and these bubbles will grow further [31]. The fractional distribution of the desorption regions of ZrH_2, ZrH_2 with 4% and ZrH_2 with 9% Y films are shown in Fig. 8. It can be seen that as the amount of yttrium doping increases from 0% to 4%, the release of helium begins in Zone II, and the release amount increases from 4.36% to 13%. When the yttrium doping amount reaches 9%, almost 50% of the helium is released in Zone II. During the heating process of the films, the interstitial helium atoms will dissociate at lower temperatures due to their lower diffusion activation energy. The helium bubbles accumulated at the grain boundaries which can act as crystal defects will first aggregate to a higher concentration. A helium bubble release network is formed at the grain boundaries of the crystal for helium release, so the helium atoms at the grain boundaries have a lower diffusion activation energy than the helium atoms inside the grains. In Fig. 8, the increased helium release fraction for ZrH_2–4Y and ZrH_2–9Y in Zone II is attributed to the existence of yttrium atoms in the ZrH_2 matrix. From the XRD

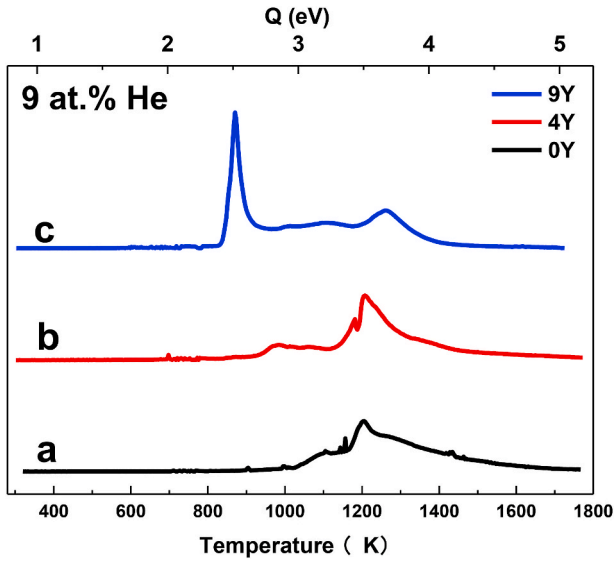

Fig. 7. Thermal desorption spectra of ZrH_2 and yttrium-doped ZrH_2 alloy films with about 9 at.% helium deposited on Mo substrates at 0.8 Pa.

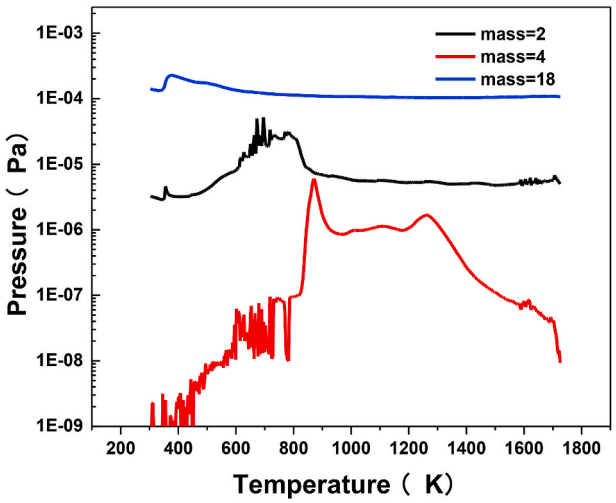

Fig. 6. Thermal desorption spectra of residual gas of different mass within yttrium-doped ZrH_2 alloy films in vacuum.

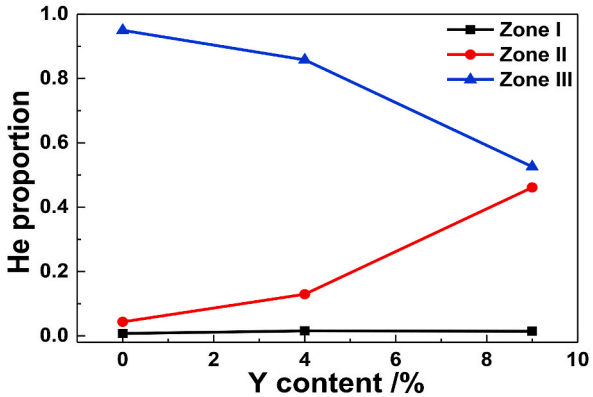

Fig. 8. The helium proportion in each desorption zones in the ZrH_2, 4%Y and 9%Y doped ZrH_2 films.

results in Fig. 5 the diffraction peaks are significantly broadened as the doping amount of yttrium in the ZrH_2 film increases. This indicates that the doping of yttrium will decrease the size of the ZrH_2 crystal grains and cause the formation of more grain boundaries [32], and the grain boundaries as the crystal defect have a strong trapping effect on the helium atoms in the matrix. When the temperature reaches the temperature around 800K–1100K at which the helium is released at the grain boundaries, these helium atoms will release rapidly through the helium bubble release network at the grain boundaries [33]. Tunes et al.'s TEM results show that when the temperature reaches 1148K, the formation of a helium bubble network can be observed in the ZrH matrix [34]. According to Taylor et al.'s TEM results, it is found that the network of helium bubbles will appear in defect areas such as grain boundaries [35]. These results are also very similar to our Zone II results that with the increase of grain boundaries, the formation of networks is easier, therefore, the formation of helium bubble networks occurs at lower temperatures. In Zone III, as the amount of yttrium doping increases, the release peak gradually moves to a higher temperature: the main peaks at 1201K (ZrH_2), 1207K (ZrH_2–4%Y), and 1262K (ZrH_2–% 9Y) are responsible to the dissociation Energies of 3.45eV, 3.5eV and 3.7eV, respectively. According to the experimental and simulation results [36], the larger the helium bubble size inside the crystal grain, the lower the temperature is required for the helium desorption. Based on the above results of thermal desorption in Zone II and XRD patterns, it can be concluded that the grain size of ZrH_2 located in the films deceases together with the formation of more grain boundaries after the doping of yttrium element. During the evolution of He, it preferably combines with the grain boundaries who act as defects and forms the helium-vacancy composites. With the increase of Y-doping, increased grain boundaries will trap more helium. Therefore, relative to ZrH_2 without Y-doping, the relative content of He within the crystalline grain bulks can be effectively inhibited and decreased He bubble sizes can be achieved for Y-doped ZrH_2 with similar amount of helium. This causes the number of helium atoms inside the crystal grains to decrease, eventually resulting in a smaller size of the bubbles in the crystal grains.

In order to study the effect of yttrium doping amount on the zirconium hydride film, the positron annihilation analysis of zirconium hydride film samples with different yttrium doping concentrations is carried out. Positrons of different energies (0.5keV–20keV) are incident on the sample, and the defect information of the sample at different depths can be measured. The distribution of S parameter profiles is shown in Fig. 9. S parameter is defined as a fraction of the central region of the positron annihilation peak (0.511 keV) [37]. When a positron is incident on the film material, it is very easy to interact with the crystal defect where the positron beam is unfolded in the film material. Thus, most of the quenching information comes from the position of the crystal defect in the sample. It can be seen in Fig. 9 that as the content of yttrium increases in the zirconium hydride matrix, defects in the material also increase. When the yttrium doping amount increases from 0 to 9%, the corresponding S parameter of the sample increases from 0.476 to 0.480. This indicates that the formation of the Y–O complex dissolved in the zirconium hydride matrix causes an increase in defect amounts in the material. As can be seen from the XRD results in Fig. 5, the zirconium hydride has the lowest surface energy on the (111) plane before the yttrium doping, therefore, there is a clear preferred orientation at the (111) lattice plane [38]. With the incorporation of yttrium, the preferred orientation of ZrH_2 film changes, indicating that the formation energy of the Zr–H system increases, which causes the crystallinity in the sample to decrease.

In order to investigate the effect on mechanical properties by doping yttrium, the hardness and elastic modulus of zirconium hydride with different yttrium concentration through nanoindentation are shown in Fig. 10. For zirconium hydride without the yttrium doping, the hardness and the elastic modulus were 10.46 ± 0.29 GPa and 116.36 ± 2.02 GPa, respectively. With the introduction of the yttrium doping, the hardness and the elastic modulus increased significantly. When the doping amount reached 9%, the hardness and elastic modulus of the sample were 12.88 ± 0.20 GPa and 136.16 ± 1.05 GPa, respectively. The corresponding increase is about 23.1% and 17% compared to ZrH_2.

4. Conclusions

IBA, XRD, TDS and PAS were used to study the effect of yttrium doping on the evolution and release characteristics of helium in zirconium hydride. The XRD results show that the introduction of hydrogen causes a large amount of dissolution of the yttrium atoms which are originally insoluble in the zirconium matrix. In the thermal desorption experiment, the release of helium occurring near 900 K is due to the incorporation of yttrium. When the doping amount of yttrium reaches 9%, almost half of the helium atoms is released in Zone II (800K–1100K). The 900K release peak corresponds to the helium atoms existing at the grain boundaries. Combining the XRD results, it can be known that the yttrium doping facilitates the zirconium hydride to form more grain boundaries, and the grain boundaries acting as crystal defects have a strong trapping effect on the helium. Moreover, the results of nanoindentation show that the yttrium doping can improve the hardness and elastic modulus of zirconium hydride due to fine grain strengthening.

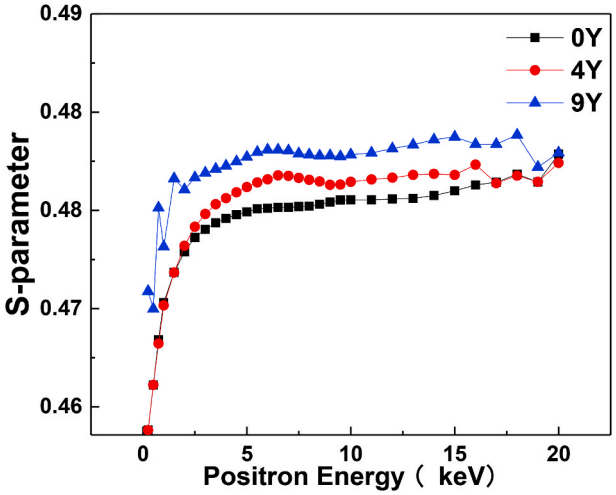

Fig. 9. The S-parameter as a function of positron implantation energy for Y-doped ZrH_2 films with different yttrium doping content and 9 at.% of helium.

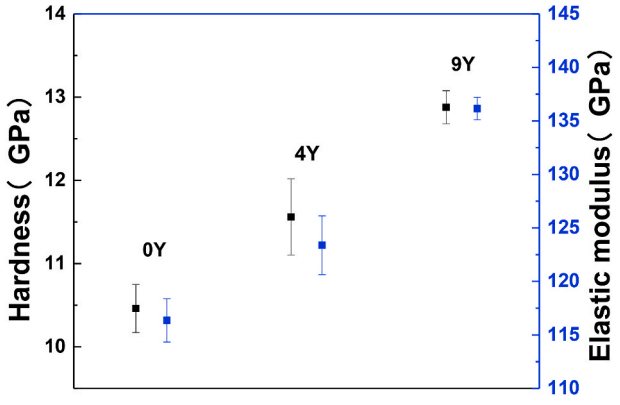

Fig. 10. The hardness and elastic modulus of helium-containing ZrH_2 and helium-containing Y-doped ZrH_2 films with a thickness of about 2 μm on Si substances.

Declaration of competing interest

We declare that we do not have any commercial or associative interest that represents a conflict of interest in connection with the work submitted.

Acknowledgements

The authors are grateful to the staff of the tandem accelerator in The Key Lab of Applied Ion Beam Physics at Fudan University, for their cooperation during ion beam analysis experiments.

References

[1] P.W. Humrickhouse, B.J. Merrill, Tritium aspects of the fusion nuclear science facility, Fusion Eng. Des. 135 (2018) 302–313.
[2] L.E. Klebanoff, J.O. Keller, 5 years of hydrogen storage research in the U.S. DOE Metal Hydride Center of Excellence (MHCoE) (vol 38, pg 4533, 2013), Int. J. Hydrogen Energy 38 (2013), 8022-8022.
[3] N.J. Dutta, S.R. Mohanty, K.P. Sooraj, M. Ranjan, Surface and structural analyses of helium ion irradiated beryllium, Vacuum 170 (2019) 108962.
[4] A. Kozlovskiy, I. Kenzhina, K. Dukenbayev, M. Zdorovets, Influence of He-ion irradiation of ceramic AlN, Vacuum 163 (2019) 45–51.
[5] B.L. Liu, S. Liu, L.B. Wang, Investigation on helium bubbles shape in Ti and Ti alloy by transmission electron microscopy, Atomic Energy Sci. Technol. 42 (2008) 799–803.
[6] L. Vincent, T. Sauvage, G. Carlot, P. Garcia, G. Martin, M.F. Barthe, P. Desgardin, Thermal behaviour of helium in silicon carbide: influence of microstructure, Vacuum 83 (2009) S36–S39.
[7] B.S. Li, Y.Y. Du, Z.G. Wang, K.F. Wei, H.P. Zhang, C.F. Yao, H.L. Chang, J.R. Sun, M.H. Cui, Y.B. Sheng, L.L. Pang, Y.B. Zhu, X. Gao, P. Luo, H.P. Zhu, J. Wang, D. Wang, Transmission electron microscopy investigations of bubble formation in He-implanted polycrystalline SiC, Vacuum 113 (2015) 75–83.
[8] A. Escudeiro, N.M. Figueiredo, T. Polcar, A. Cavaleiro, Structural and mechanical properties of nanocrystalline Zr co-sputtered a-C(:H) amorphous films, Appl. Surf. Sci. 325 (2015) 64–72.
[9] I.S. Batra, R.N. Singh, P. Sengupta, B.C. Maji, K. Madangopal, K.V. Manikrishna, R. Tewari, G.K. Dey, Mitigation of hydride embrittlement of zirconium by yttrium, J. Nucl. Mater. 389 (2009) 500–503.
[10] Q. Wan, X. Bai, X. Liu, Impact of yttrium ion implantation on corrosion behavior of laser beam welded zircaloy-4 in sulfuric acid solution, Appl. Surf. Sci. 252 (2005) 1974–1980.
[11] C. Li, L. Xiong, E. Wu, S. Liu, Effect of yttrium on nucleation and growth of zirconium hydrides, J. Nucl. Mater. 457 (2015) 142–147.
[12] J.C. Zhang, E.D. Wu, S. Liu, Effects of Y on helium behavior in Ti-Y alloy films, J. Nucl. Mater. 454 (2014) 119–125.
[13] E. Markina, M. Mayer, H.T. Lee, Measurement of He and H depth profiles in tungsten using ERDA with medium heavy ion beams, Nucl. Instrum. Methods Phys. Res. Sect. B Beam Interact. Mater. Atoms 269 (2011) 3094–3097.
[14] F. Schiettekatte, A. Chevarier, N. Chevarier, A. Plantier, G.G. Ross, Quantitative depth profiling of light elements by means of the ERD ExB technique, Nucl. Instrum. Methods Phys. Res. Sect. B Beam Interact. Mater. Atoms 118 (1996) 307–311.
[15] M. Mayer, SIMNRA, Max-Planck-Institut für Plasmaphysik, Garching, Version 6.03.
[16] G. Vaggelli, A. Borghi, R. Cossio, C. Mazzoli, F. Olmi, Comparison between major and trace element concentrations in garnet performed by EPMA and micro-PIXE techniques, Spectrochim. Acta, Part B 58 (2003) 699–709.
[17] J.L. Campbell, T.L. Hopman, J.A. Maxwell, Z. Nejedly, The Guelph PIXE software package III: alternative proton database, Nucl. Instrum. Methods B 170 (2000) 193.
[18] Z.B. Han, C.J. Wang, L.Q. Shi, Synthesis and characterization of helium-charged titanium hydride films deposited by direct current magnetron sputtering with mixed gas, Mater. Des. 119 (2017) 180–187.
[19] JCPDS,05-0665.
[20] JCPDS, 43-0661.
[21] JCPDS,34-0649.
[22] Z.B. Han, G.J. Cheng, L.Q. Shi, Synthesis and characterization of Y-doped TiH2 films prepared by magnetron sputtering, Int. J. Hydrogen Energy 41 (2016) 2820–2828.
[23] JCPDS,41-1120.
[24] Z. Han, C. Wang, G. Cheng, H. Zhang, R. Su, Y. Duan, J. Gao, X. Ni, B. Ye, W. Zhang, L. Shi, Effects of Y on helium behavior in Y-doped TiH2 films prepared by magnetron sputtering, J. Alloy, Compd 744 (2018) 778–784.
[25] E. Oliviero, M.F. Beaufort, J.F. Barbot, A. van Veen, A.V. Fedorov, Helium implantation defects in SiC: a thermal helium desorption spectrometry investigation, J. Appl. Phys. 93 (2003) 231–238.
[26] Y.F. Lu, L.Q. Shi, W. Ding, X.G. Long, First-principles study of hydrogen impact on the formation and migration of helium interstitial defects in hcp titanium, Chin. Phys. Lett. 29 (2012), 013102.
[27] B.S. Li, C.H. Zhang, H.H. Zhang, T. Shibayama, Y.T. Yang, Study of the damage produced in 6H-SiC by He irradiation, Vacuum 86 (4) (2011) 452–456.
[28] H. Zhang, R. Su, D. Chen, L. Shi, Thermal desorption behaviors of helium in Zr-Co films prepared by sputtering deposition method, Vacuum 130 (2016) 174–178.
[29] T. Seletskaia, Y.N. Osetsky, R.E. Stoller, G.M. Stocks, Calculation of helium defect clustering properties in iron using a multi-scale approach, J. Nucl. Mater. 351 (2006) 109–118.
[30] P.N. Ma, L. Pollet, M. Troyer, F.C. Zhang, A classical picture of the role of vacancies and interstitials in Helium-4, J. Low Temp. Phys. 152 (2008) 156–163.
[31] J. Gao, L.M. Bao, H.F. Huang, Y. Li, J.R. Zeng, Z. Liu, R.D. Liu, L.Q. Shi, Evolution law of helium bubbles in hastelloy N alloy on post-irradiation annealing conditions, Materials 9 (2016) 5.
[32] G. Panomsuwan, O. Takai, N. Saito, Controlled crystalline orientation of SrTiO3 thin films grown on Pt(111)/Ti/α-Al2O3(0001) substrates: effect of growth temperature and Ti layer thickness, Appl. Surf. Sci. 309 (2014) 95–105.
[33] C.S. Snow, J.F. Browning, G.M. Bond, M.A. Rodriguez, J.A. Knapp, He-3 bubble evolution in ErT2: a survey of experimental results, J. Nucl. Mater. 453 (2014) 296–306.
[34] M.A. Tunes, R.W. Harrison, G. Greaves, J.A. Hinks, S.E. Donnelly, Effect of He implantation on the microstructure of zircaloy-4 studied using in situ TEM, J. Nucl. Mater. 493 (2017) 230–238.
[35] C. Taylor, K. Hattar, B. Arey, B. Matthews, D. Zschiesche, R. Goeke, Investigation of helium behavior in multilayered hydride structures through in-situ TEM ion implantation, Microsc. Microanal. 25 (2019) 1570–1571.
[36] J. Wang, Q. Hou, Molecular dynamics simulation of helium cluster growth in titanium, Acta Phys. Sin. 58 (2009) 6408–6412.
[37] Q. Li, Y. Wang, J. Liu, W. Kong, B. Ye, Structural and magnetic properties in Mn-doped ZnO films prepared by pulsed-laser deposition, Appl. Surf. Sci. 289 (2014) 42–46.
[38] C. Wang, Q. Hu, J. Huang, C. Zhu, Z. Deng, H. Shi, L. Wu, Z. Liu, Y. Cao, Enhanced hydrogen production by water splitting using Cu-doped TiO2 film with preferred (001) orientation, Appl. Surf. Sci. 292 (2014) 161–164.